Hyperpolarized Carbon 13 MRI: Clinical Applications and Future Directions in Oncology

Surrin S. Deen, MBBS, PhD • Catriona Rooney, BSc • Ayaka Shinozaki, MPhil • Jordan McGing, PhD • James T. Grist, PhD • Damian J. Tyler, MD, PhD • Eva Serrão, MD, PhD • Ferdia A. Gallagher, BM BCh, PhD

From the Department of Radiology, Cambridge University Hospitals, Biomedical Campus, Cambridge, CB2 0QQ, England (S.S.D., E.S., F.A.G.); Department of Physiology, Anatomy, and Genetics (C.R., A.S., J.T.G., D.J.T.) and the Oxford Centre for Clinical Magnetic Resonance Research (A.S., J.T.G., D.J.T.), University of Oxford, Oxford, England; Department of Radiology, Oxford University Hospitals, Oxford, England (J.M., J.T.G.); Institute of Cancer and Genomic Sciences, University of Birmingham, Birmingham, England (J.T.G.); Department of Radiology, University of Cambridge, Cambridge, England (E.S., F.A.G.); Cancer Research UK Cambridge Centre, Cambridge, England (F.A.G.); and Joint Department of Medical Imaging, University Health Network, University of Toronto, Toronto, Canada (E.S.). Received January 24, 2023; revision requested February 28; revision received June 16; accepted August 2. **Address correspondence to** S.S.D. (email: *surrin.deen@stcatz.ox.ac.uk*).

Supported by Cancer Research UK (CRUK), the CRUK Cambridge Centre, the Mark Foundation for Cancer Research, the Gates Cambridge Foundation, the National Institute of Health Research-Cambridge Biomedical Research Centre, The Medical Research Council (MRC), Addenbrooke's Charitable Trust, and the Cambridge Experimental Cancer Medicine Centre.

Conflicts of interest are listed at the end of this article.

Hyperpolarized carbon 13 MRI (^{13}C MRI) is a novel imaging approach that can noninvasively probe tissue metabolism in both normal and pathologic tissues. The process of hyperpolarization increases the signal acquired by several orders of magnitude, allowing injected ^{13}C-labeled molecules and their downstream metabolites to be imaged in vivo, thus providing real-time information on kinetics. To date, the most important reaction studied with hyperpolarized ^{13}C MRI is exchange of the hyperpolarized ^{13}C signal from injected [1-^{13}C]pyruvate with the resident tissue lactate pool. Recent preclinical and human studies have shown the role of several biologic factors such as the lactate dehydrogenase enzyme, pyruvate transporter expression, and tissue hypoxia in generating the MRI signal from this reaction. Potential clinical applications of hyperpolarized ^{13}C MRI in oncology include using metabolism to stratify tumors by grade, selecting therapeutic pathways based on tumor metabolic profiles, and detecting early treatment response through the imaging of shifts in metabolism that precede tumor structural changes. This review summarizes the foundations of hyperpolarized ^{13}C MRI, presents key findings from human cancer studies, and explores the future clinical directions of the technique in oncology.

An earlier incorrect version appeared online. This article was corrected on September 8, 2023

MRI is a powerful clinical tool that provides a range of image contrast mechanisms to assist in the identification and evaluation of tumors. Many of these contrast mechanisms exploit fundamental biologic differences between cancer and normal tissue and use the signal generated from molecular protons (or hydrogen nuclei [^{1}H]), which provide the highest signal of any naturally occurring nucleus. Other nuclei such as carbon could provide unique information on tissue biochemistry but yield extremely low signal with conventional MRI techniques. Most of the carbon in the human body is in the form of the carbon 12 (^{12}C) isotope, which is not detectable at MRI, while approximately 1.1% of naturally occurring carbon is in the magnetically active form of carbon 13 (^{13}C). As a result, the signal from naturally abundant ^{13}C is very low. One method for overcoming the low signal of ^{13}C MRI is through the external hyperpolarization and injection of exogenous ^{13}C-labeled molecules, thereby enabling the imaging of central metabolic pathways such as glycolysis and the tricarboxylic acid cycle in real time.

Hyperpolarization by Dynamic Nuclear Polarization

Hyperpolarization refers to a temporary increase in the proportion of nuclear spins aligned with the main magnetic field (B_0). There are numerous techniques that can be used to achieve hyperpolarization, one of which is dynamic nuclear polarization. Dynamic nuclear polarization involves the cooling of a ^{13}C-enriched sample together with an electron-rich compound (electron paramagnetic agent) close to absolute zero (approximately 1 K) in the presence of a strong magnetic field (3.35–7 T) for approximately 2 hours. These extreme physical conditions cause the electrons in the mixture to approach unity polarization. Following irradiation of the sample with microwaves, the electron polarization is transferred to the ^{13}C nuclei in the molecule of interest, thus increasing the detectable signal. In 2003, a breakthrough publication demonstrated that dynamic nuclear polarization increased the signal-to-noise ratio of ^{13}C imaged using MR spectroscopy by more than 10 000-fold. It was also shown that the frozen sample could subsequently be dissolved into liquid form for injection while maintaining polarization levels that decay with a spin lattice relaxation time (T_1) of approximately 50–70 seconds ex vivo and 20–30 seconds in vivo (1). This advance meant that the dissolved hyperpolarized ^{13}C-labeled molecule could be injected into biologic systems and detected with a higher sensitivity, allowing for the investigation of in vivo metabolism.

Although alternative methods for ^{13}C hyperpolarization such as parahydrogen-induced polarization have been described, no clinical ^{13}C hyperpolarizer device using any method other than dynamic nuclear polarization has been developed to date. Techniques such as spin-exchange optical pumping and metastability-exchange optical pumping have, however, been used for clinical ventilation imaging with hyperpolarized helium 3 and xenon 129 gas (2).

Abbreviations

FDG = fluorodeoxyglucose, k_{PL} = apparent exchange rate constant for LDH, LDH = lactate dehydrogenase, MCT = monocarboxylate transporter, NADH = reduced nicotinamide adenine dinucleotide, NAD$^+$ = oxidized NAD, PARP = poly (adenosine diphosphate–ribose) polymerase

Summary

Clinical hyperpolarized carbon 13 MRI has been shown to identify occult tumors, stratify lesions based on histologic grade, and detect early response to treatment in several cancers, suggesting its potential to improve cancer care in the future.

Essentials

- Hyperpolarized carbon 13 (^{13}C) pyruvate MRI is an emerging technique for imaging tissue metabolism that has been translated into the clinic, with initial human studies showing that it correlates with important biologic properties of tissue, including hypoxia.
- In many cancers, the formation of labeled tissue lactate from the injected pyruvate can be used to identify multifocal disease that is occult on proton MR images, as well as to determine tumor grade and detect early response to treatment.
- Clinical research is ongoing to validate the biologic significance of the signal acquired with hyperpolarized ^{13}C pyruvate in humans, to further verify repeatability and reproducibility, and to evaluate accuracy of the method for monitoring response to new targeted anticancer drugs.
- Future technical developments are required to enable ease of use in radiology departments so that larger studies can be undertaken to assess clinical feasibility and advantages of hyperpolarized ^{13}C pyruvate MRI compared with other metabolic imaging techniques, such as fluorine 18 fluorodeoxyglucose PET/CT.

Keywords

Hyperpolarized Carbon 13 MRI, Molecular Imaging, Cancer, Tissue Metabolism

Technical Considerations in Clinical Imaging

Currently, clinical hyperpolarized ^{13}C MRI is largely focused on using hyperpolarized ^{13}C-labeled pyruvate as a tracer, where the first carbon position is labeled with the ^{13}C isotope ([1-^{13}C] pyruvate). This is due to the favorable physical and chemical properties of [1-^{13}C]pyruvate for hyperpolarization and the central biochemical role of pyruvate, which means ^{13}C can be detected after incorporation of the label into several important metabolic reactions in both normal tissue and cancer (3). Although the use of many hyperpolarized ^{13}C molecules in addition to pyruvate has been reported, the majority of these molecules are used only in preclinical models. However, there is ongoing research into the clinical translation and application of hyperpolarized molecules such as [2-^{13}C]pyruvate for assessing tricarboxylic acid intermediates, fumarate for imaging necrosis, and urea for perfusion imaging (4–7).

A custom imaging setup is required for clinical hyperpolarized [1-^{13}C]pyruvate MRI where the hyperpolarizer is sited outside of the MRI room, but rapid transfer of the sample between the hyperpolarizer and scanner is still allowed to minimize the time between sample dissolution and imaging during which the hyperpolarized state decays. The hyperpolarized sample must also undergo rapid quality control checks before clinical use, which includes measurements of pyruvate concentration, pH, residual radical levels, and temperature, as well as passing through a sterilized filter. A dedicated MRI coil sensitive to ^{13}C is required to transmit and detect the signal, and the scanner must have multinuclear capabilities so that anatomic ^{1}H images can be produced to assist with interpretation of the ^{13}C images.

Due to the relatively low ^{13}C signal and to facilitate spectral separation of the signals from each metabolite, a 3-T field strength MRI machine is typically used. The choice of the best magnetic field strength for hyperpolarization studies is complicated by the nonlinear relationship between the T1 relaxation time and magnetic field strength. Field strengths above 3 T have not yet been investigated in a clinical setting but may lead to greater dephasing of the hyperpolarized state and chemical shift artifact.

The rapid decay of the ^{13}C signal necessitates the use of a fast acquisition pulse sequence. Following dissolution, sufficient signal for detection is present for only approximately five times the T1 of ^{13}C, which is equivalent to a few minutes. During this short time frame, the hyperpolarized solution must be transferred to the scanner, be injected intravenously into the patient, perfuse to the region of interest in the body, and undergo cellular uptake and metabolism within the tissue. Therefore, hyperpolarized ^{13}C MRI is particularly suited to imaging rapid chemical reactions.

In the clinical setting, fast gradient-echo approaches with either a spiral or echo-planar imaging readout are used, although echo-planar imaging has some disadvantages because it may produce artifacts, including frequency shift artifacts, geometric distortion artifacts, and Nyquist ghost artifacts (8). The readouts are coupled either with spectral-spatial radiofrequency pulses or iterative decomposition of water and fat with echo asymmetry and least-squares estimation (ie, IDEAL) encoding to provide temporally resolved multisection or three-dimensional imaging (9). Although these imaging approaches usually require physicist support, they are increasingly being made available as part of multinuclear packages that can be implemented on routine clinical systems.

Initial Human Imaging, Methods, and Safety

The first human study investigating hyperpolarized [1-^{13}C]pyruvate MRI in cancer was published in 2013 and established the safety of the tracer, prepared using a prototype clinical hyperpolarizer device, and the method of delivery in patients with prostate cancer. In this proof-of-concept study, high prostatic [1-^{13}C]lactate signal was demonstrated in a patient who had no abnormal signal intensity on conventional proton MR images. When this region of high signal intensity was subsequently biopsied, it was found to represent a low-grade tumor (10). These results provided initial evidence that clinical hyperpolarized [1-^{13}C]pyruvate MRI could depict some tumors that are occult on conventional ^{1}H MR images.

The prototype clinical polarizer was subsequently developed into a commercial clinical hyperpolarizer, termed a SPINlab (GE Research Circle Technology), which can be easily sited within a radiology department and includes automated dissolution and

quality control checks. A sterile fluid path or pharmacy kit was designed for use with the SPINlab as a single-use, disposable unit containing the chemical components required to hyperpolarize and dissolve a sample before delivery into the patient. The path must be assembled and filled in a clean room or pharmacy environment, with the details of the approach dependent on the local and national regulatory framework under which the work is being undertaken. The first human study reported injection of tracer at a pH of 7.3–8.0, temperatures of 28.8°–36.4°C, and volumes of 31.9–53.5 mL with no major adverse events (10). Typically, approximately 250 mM of hyperpolarized [1-¹³C] pyruvate is injected at 0.4 mL/kg at a rate of 5 mL/sec using a power injector, followed by a 25-mL saline flush. At present, spatial resolution is at around 1 × 1 × 1 cm for most tumors.

Clinical Data Analysis

The analysis of hyperpolarized [1-¹³C]pyruvate spectra includes analysis of the pyruvate and lactate peak intensities within a region of interest dynamically over time, similar to the approaches used in modeling PET or dynamic contrast-enhanced MRI data. For example, with hyperpolarized [1-¹³C]pyruvate MRI, the modeled parameter k_{PL} represents the apparent exchange rate constant for the enzyme lactate dehydrogenase (LDH), which serves as a marker for cytosolic nonoxidative metabolism, and can be derived from the fitting of kinetic parameters to an exchange model mathematically. In comparison, the area under the receiver operating characteristic curve of the lactate-to-pyruvate ratio represents a simple surrogate of metabolic activity. Exchange models can be time-consuming to calculate and very sensitive to the early parameter values in the model (11), whereas the area under the receiver operating characteristic curve methods have the advantage of being independent of the shape of pyruvate inflow (12). There is a movement in the radiology community to develop a best-practice approach for the analysis of data sets, and the comparison of models with different imaging setups is an important area of current and future research.

Clinical Applications of Hyperpolarized [1-¹³C] Pyruvate MRI in Oncology

Metabolic Profiling of Tumors

Malignant transformation is associated with a metabolic shift in the cellular handling of glucose which manifests as an increase in glucose uptake, glycolysis, and lactate formation. Tumor cells generate substantial amounts of lactate even in the presence of oxygen, partly due to the anabolic demands of rapid proliferation (13), and this phenomenon is referred to as aerobic glycolysis or the Warburg effect. Both fluorine 18 fluorodeoxyglucose (¹⁸F-FDG) PET and hyperpolarized ¹³C MRI can be used to investigate these changes in glucose metabolism, although at different levels in the metabolic pathways (14). Furthermore, while ¹⁸F-FDG PET allows for only a combined signal to be detected from the labeled glucose analog and its phosphorylated product, individual hyperpolarized ¹³C-labeled molecules can be discriminated using MR spectroscopy. Following injection of hyperpolarized [1-¹³C]pyruvate, the hyperpolarized signal can be detected from the injected pyruvate

and its products (lactate, bicarbonate, and alanine) depending on the tissue being imaged and the nature of the disease. The major metabolic pathways relevant to hyperpolarized [1-¹³C] pyruvate MRI are summarized in Figure 1.
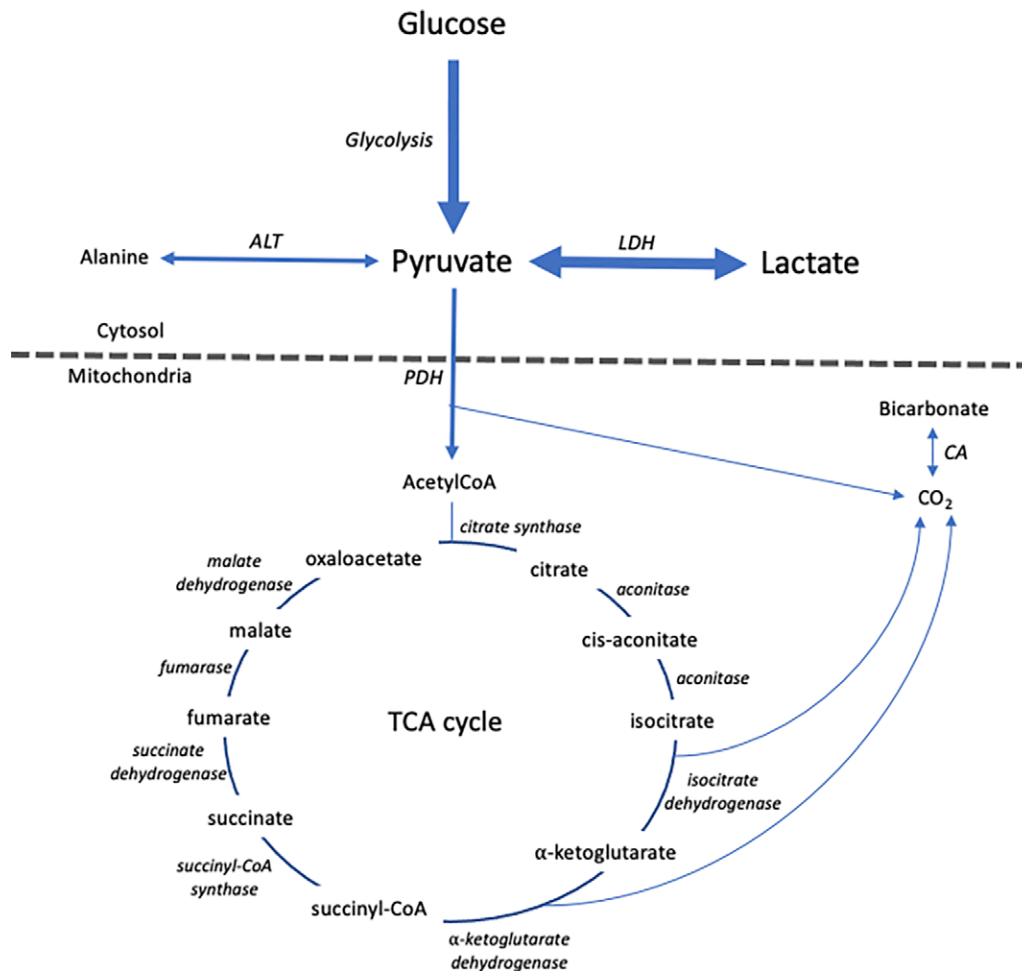
Metabolism of hyperpolarized [1-¹³C]pyruvate to hyperpolarized [1-¹³C]lactate has now been demonstrated in humans for a number of tumors, including those of the prostate, pancreas, kidney, breast, and brain (15–19). Figure 2 shows an example of hyperpolarized [1-¹³C]pyruvate being metabolized into lactate and bicarbonate in a glioblastoma. The figure additionally demonstrates the metabolic heterogeneity within the tumor on the maps of hyperpolarized [1-¹³C]pyruvate, hyperpolarized [1-¹³C] lactate, and hyperpolarized [1-¹³C]bicarbonate that have been summed over time (20).

The high lactic acid concentration in and surrounding tumors is not only a metabolic byproduct of increased metabolism and proliferation but is also thought to aid tumor invasion through acidification of the extracellular environment. Consequently, lactate concentration in tumors has a strong correlation with aggressiveness, metastatic potential, and overall prognosis (21–23). Evidence is now emerging that hyperpolarized [1-¹³C]lactate imaging may be able to serve as a surrogate marker of tumor grade, for example, in prostate cancer and breast cancer (18,24–26).

There are several biologic processes and tissue characteristics that may determine the hyperpolarized ¹³C MRI signal, including tracer delivery, expression of the transmembrane pyruvate transporter, and levels of the enzymes that catalyze pyruvate metabolism. Tumor perfusion, vascular density, and vascular permeability can affect the early stage in signal generation and delivery of the tracer to the organ of interest. Figure 3 shows an example of hyperpolarized [1-¹³C]pyruvate and hyperpolarized [1-¹³C]lactate images at 15 time points with 4-second gaps between them (Fig 3F and 3G) and summed (Fig 3C and 3D) in a patient with breast cancer. The T1-weighted dynamic contrast-enhanced images for comparison (Fig 3A and 3B) illustrate that gadolinium enhancement reflects vascularity and pyruvate delivery.

With hyperpolarized [1-¹³C]pyruvate MRI, as the metabolism of pyruvate is intracellular, transmembrane transport is required and facilitated by the monocarboxylate transporters (MCTs). The MCT family of transmembrane proteins transport pyruvate and lactate in both directions across the cell membrane (27,28). There are four subtypes of MCTs, 1–4, which exhibit different kinetics and substrate specificity. MCT-1 and MCT-4 have increased expression in tumors and lead to higher uptake of pyruvate and higher efflux of lactate. MCT expression has been shown to be important for the conversion of extracellular pyruvate to lactate in some cell studies (29) and several animal studies, and recent clinical work has now also demonstrated that MCT expression correlates with lactate-to-pyruvate signal ratio in humans (18,26,30,31).

Tumor activity of the enzyme LDH is another key determinant of the rate of conversion of pyruvate into lactate and therefore the hyperpolarized [1-¹³C]lactate signal. LDH activity, and specifically the expression of the LDH-A subunit, is higher in most tumor subtypes compared with healthy tissue (32–35). The metabolism of hyperpolarized [1-¹³C]pyruvate has been

Figure 1: Simplified schematic of the major metabolic pathways that can be investigated with hyperpolarized [1–carbon 13] pyruvate MRI. ALT = alanine transaminase, CA = carbonic anhydrase, CoA = coenzyme A, LDH = lactate dehydrogenase, PDH = pyruvate dehydrogenase, TCA = tricarboxylic acid.

correlated with the increased expression of LDH in human prostate cancer, breast cancer, and glioblastoma (16,30,20)

Several hyperpolarized [1-^{13}C]pyruvate MRI studies have shown that increased ^{13}C lactate signal may be related to LDH and MCT expression, and that there are differences in the importance of these molecules between tumors (18,20,30). One human breast cancer study also showed that lactate formation may additionally be driven by tumor hypoxia as ^{13}C signal correlated with expression of hypoxia inducible factor (HIF)–1α, a transcription regulator that is dependent on oxygen tension (18).

There are multiple new anticancer drugs that target MCT, HIF-1α pathways, and even LDH activity (36–39). Hyperpolarized [1-^{13}C]pyruvate MRI could find a role in the metabolic profiling of tumors to identify possible patient candidates for these types of drugs in the future.

Tumor Stratification: Assessment of Disease Aggression and Grade

Clinical results have now demonstrated that hyperpolarized [1-^{13}C]pyruvate MRI findings can stratify tumors according to grade, with higher grade lesions producing higher hyperpolarized lactate signal intensity (25). For example, in prostate cancer, hyperpolarized [1-^{13}C]pyruvate MRI findings were shown to identify intermediate-risk subtypes not detectable with ^{1}H MRI (16,26). In clear cell renal cell carcinoma, hyperpolarized [1-^{13}C]pyruvate MRI revealed intratumoral metabolic heterogeneity and was found to act as a surrogate for grade and potentially outcome (17,31). Figure 4 depicts results of a study on renal cell carcinoma confirming an increase in hyperpolarized ^{13}C signal in higher grade tumors, with the grade 4 tumor producing the highest pyruvate, lactate, and k_{PL}, followed by the grade 3 and grade 2 tumors (31).

Early Diagnosis and Earlier Detection of Successful Response to Treatment

During malignant transformation, metabolic changes precede structural and functional changes as glucose is diverted away from aerobic metabolism to provide the larger molecular building blocks required to support cell growth and division in the tumor. These biochemical changes may be detected with metabolic imaging before conventional imaging-based treatment response assessment criteria such as the Response Evaluation Criteria in Solid Tumors, or RECIST. Clinical hyperpolarized
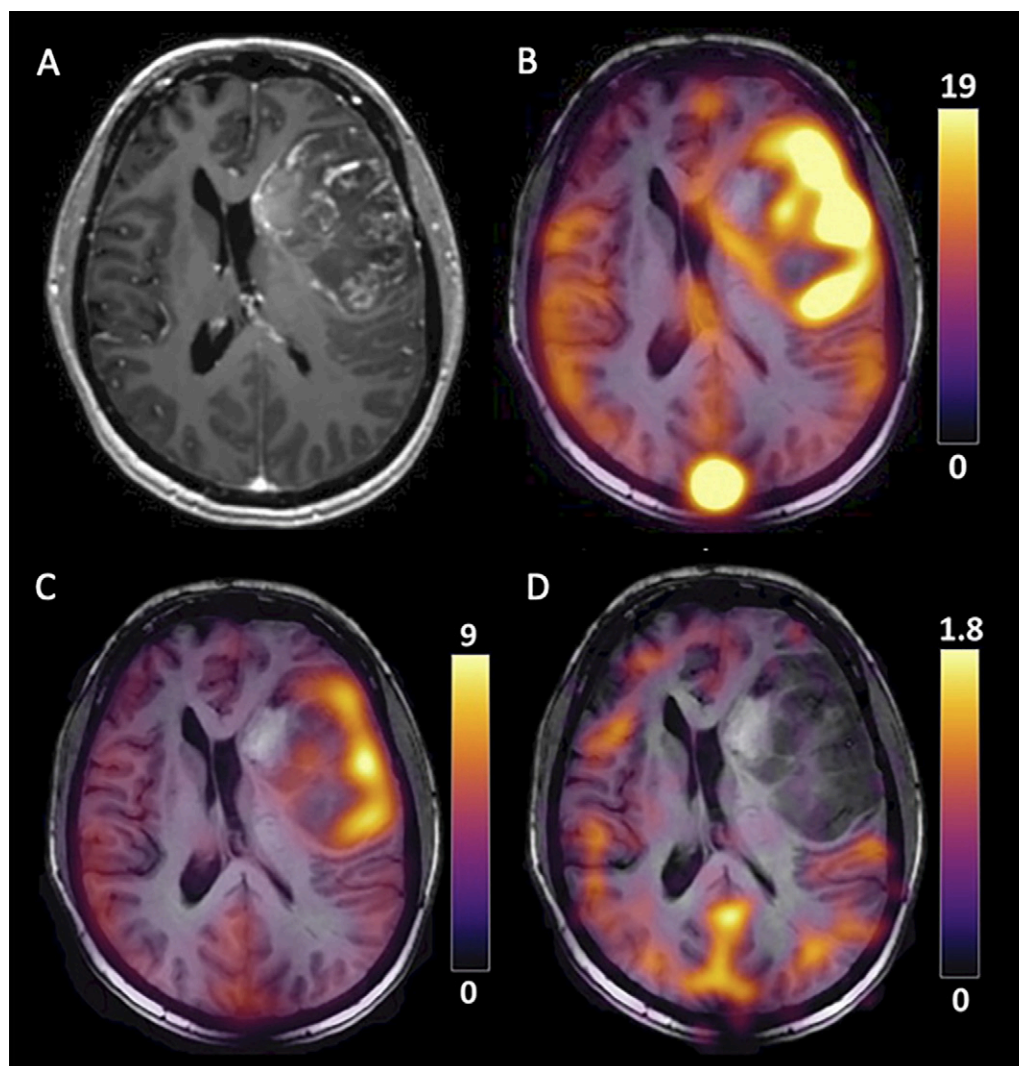
Figure 2: Hyperpolarized carbon 13 MR images in a patient with glioblastoma that demonstrate heterogeneity in metabolism. **(A)** Axial contrast-enhanced T1-weighted fast spoiled gradient-echo image through the center of the lesion and **(B)** overlaid with the pyruvate, **(C)** lactate, and **(D)** bicarbonate color maps all summed over the imaging time course. (Reprinted, under a CC BY 4.0 license, from reference 20.)
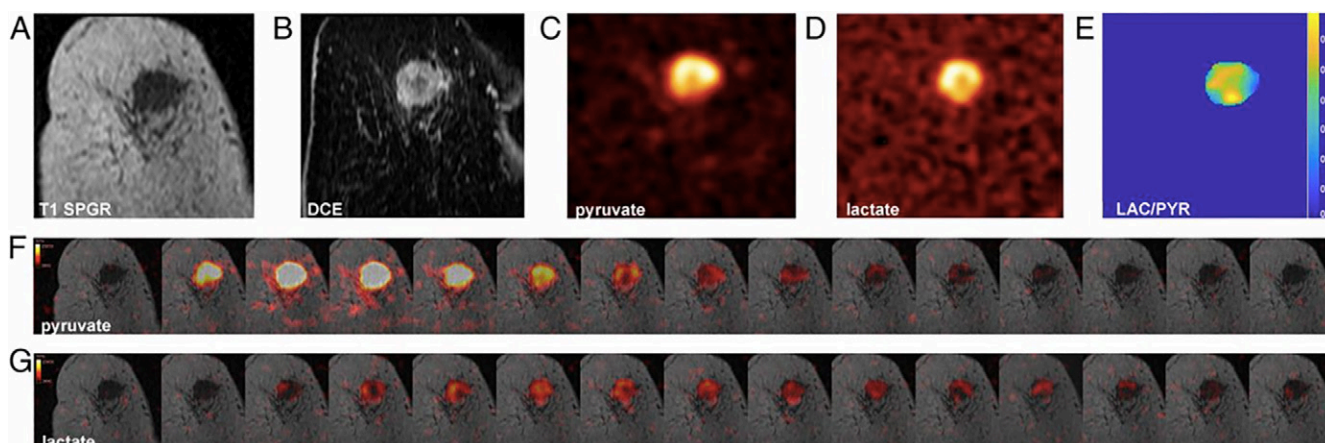
Figure 3: Hyperpolarized [1–carbon 13]pyruvate MR images in a patient with triple-negative breast cancer. **(A)** Coronal T1-weighted three-dimensional spoiled gradient-echo (SPGR) image. **(B)** Coronal reformatted dynamic contrast-enhanced (DCE) image at peak enhancement after injection of a gadolinium-based contrast agent. **(C)** Summed hyperpolarized carbon 13 pyruvate images. **(D)** Summed hyperpolarized carbon 13 lactate images. **(E)** Lactate:pyruvate (LAC/PYR) ratio map. **(F, G)** Dynamic hyperpolarized carbon 13 pyruvate and lactate imaging with a 12-second delay after injection over 15 time points at 4-second intervals. (Reprinted, with permission, from reference 18.)
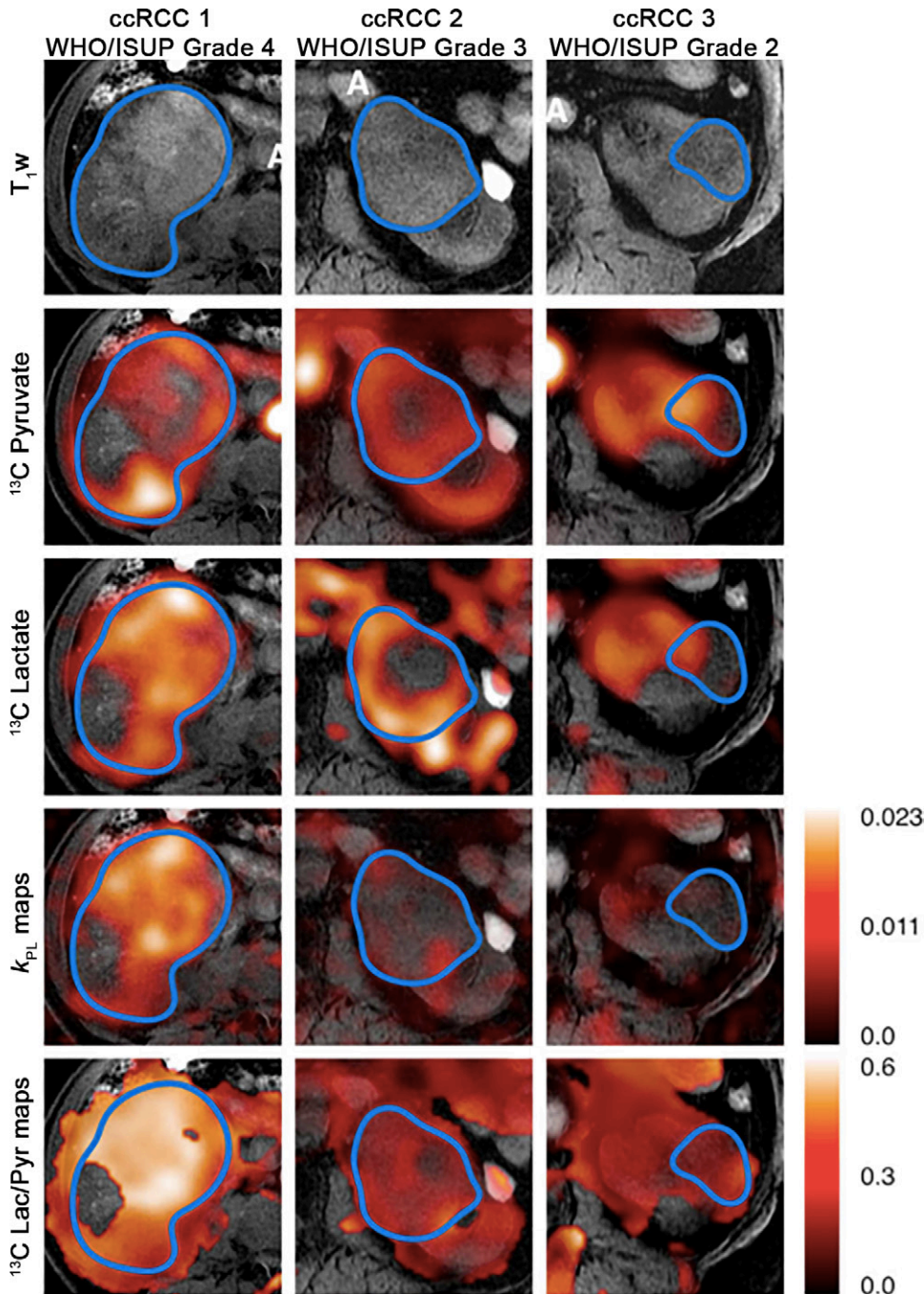
Figure 4: Carbon 13 (^{13}C) pyruvate and ^{13}C lactate signal intensity summed over all time points superimposed on an axial T1-weighted (T_1^w) image of the largest tumor cross-section for three different grade renal cell carcinomas. The border of the tumor is outlined in blue. ccRCC = clear cell renal cell carcinoma, k_{PL} = apparent exchange rate constant for lactate dehydrogenase, Lac/Pyr = lactate:pyruvate ratio, WHO/ISUP = World Health Organization/International Society of Urological Pathology. (Reprinted, under a CC BY 4.0 license, from reference 31.)

[1-^{13}C]pyruvate MRI is thought to depict the early biochemical changes of carcinogenesis and treatment response that are driven by increased pyruvate uptake, LDH activity, and lactate production. Figure 5 shows a case from a recently published study of histologically proven prostate cancer with a tumor focus in the right peripheral zone (red region of interest on histologic image) that was detectable on hyperpolarized [1-^{13}C] pyruvate MR images (red arrow) but not with proton MRI

sequences (16).

Preclinical research has shown that hyperpolarized [1-^{13}C]pyruvate MRI can depict biochemical responses to chemotherapy as early as 24 hours after treatment (40). More recently, human trials have provided initial evidence that hyperpolarized [1-^{13}C]pyruvate MRI may also depict treatment response in the clinical setting such as in breast cancer after neoadjuvant therapy (30,41). Although most preclinical studies have found a reduction in lactate labeling following successful treatment, a clinical breast cancer study in the neoadjuvant setting showed that an increase in the lactate-to-pyruvate ratio of approximately 20% occurred 7–11 days after commencing treatment and identified those patients who went on to have a pathologic complete response at surgery. Figure 6 is taken from this study and gives examples of the changes that can be observed in lactate:pyruvate ratio with hyperpolarized [1-^{13}C]pyruvate MRI following treatment of two different patients. Figure 6A and 6B depict images of a patient with human epidermal growth factor receptor 2–positive breast cancer before standard-of-care chemotherapy treatment who had a decrease in lactate:pyruvate ratio following treatment (Fig 6C and 6D), corresponding to a histologic nonresponse. Figure 6F and 6G depict baseline images of another patient with triple-negative breast cancer who had an increase in lactate:pyruvate ratio after treatment with chemotherapy and a poly (adenosine diphosphate–ribose) polymerase (PARP) inhibitor (Fig 6H and

6I), corresponding to a confirmed histologic response (30). The contrast in results between clinical and preclinical studies here was hypothesized to be due to differences in the timing of posttreatment imaging in humans compared with animals or to differences in the onset of hypoxia or immune infiltration, reflecting the importance of translational studies from animals to humans in understanding the clinical role of this new technique for response monitoring.
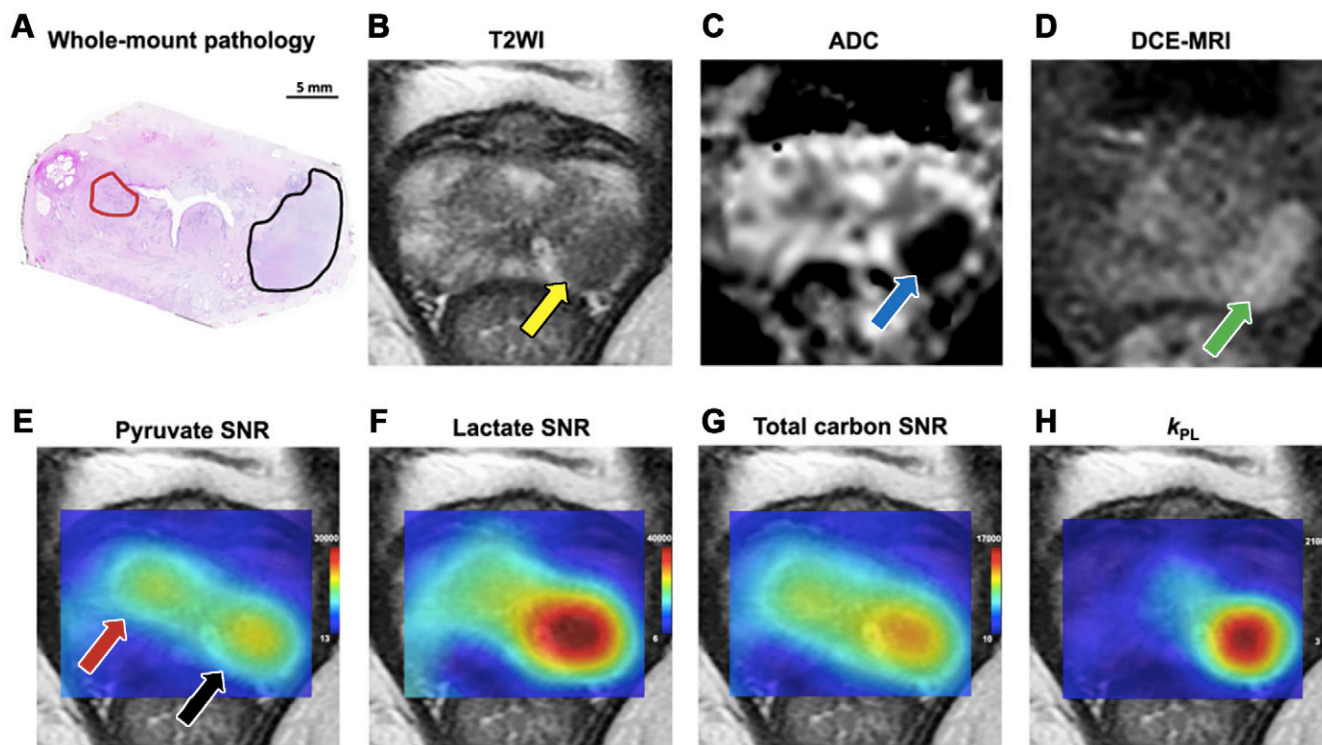
Figure 5: Images in a 64-year-old patient who underwent robot-assisted radical prostatectomy. **(A)** Postsurgical histopathologic assessment confirmed the diagnosis of adenocarcinoma of the prostate. The red region of interest represents an International Society of Urological Pathology (ISUP) grade 1 lesion in the right peripheral zone, and the black region of interest represents a ISUP grade 3 lesion in the left peripheral zone. **(B)** T2-weighted MR (T2WI) image demonstrates a single marked area of low signal intensity corresponding to the target lesion in the left peripheral zone (yellow arrow). **(C)** Apparent diffusion coefficient (ADC) map demonstrates a corresponding focus of markedly restricted diffusion in the left peripheral zone (blue arrow). **(D)** Dynamic contrast-enhanced (DCE) MR image demonstrates the area of early enhancement in the left peripheral zone (green arrow). **(E)** Pyruvate signal-to-noise ratio (SNR) map with two areas of high pyruvate signal intensity, with the red and black arrows corresponding to the grade 1 and grade 3 histopathology-confirmed tumor foci, respectively. **(F)** Lactate SNR map demonstrates high [1–carbon 13]lactate signal intensity in the left peripheral zone lesion. **(G)** Total carbon SNR map shows higher signal intensity in the left peripheral zone tumor. **(H)** The apparent exchange rate constant for lactate dehydrogenase (k_{PL}) map (presented as sec^{-1}) shows a higher rate of pyruvate-to-lactate conversion in the more aggressive left peripheral zone lesion. (Reprinted, under a CC BY 4.0 license, from reference 16.)

PARP inhibitors are a class of anticancer drugs that may be particularly suitable for imaging with hyperpolarized [1-^{13}C]pyruvate, as PARP activity depletes oxidized nicotinamide adenine dinucleotide (NAD$^+$) and reduced nicotinamide adenine dinucleotide (NADH), the cofactors for the LDH enzyme (42,43). PARP inhibition has been shown to increase lactate signal relative to pyruvate when used with standard-of-care neoadjuvant treatment in breast cancer which may be due to restoration of NAD$^+$ and NADH levels (30). Other new areas for therapy that could likely be monitored with hyperpolarized ^{13}C MRI include the effect of new cancer therapies that specifically target metabolism, as well as immunotherapy which may also indirectly modulate immune cell metabolism and increase metabolic activity (44–46).

Challenges and Future Directions for Hyperpolarized [1-^{13}C]Pyruvate MRI

Key clinical and preclinical studies investigating hyperpolarized [1-^{13}C]pyruvate MRI are listed in Tables 1 and 2, respectively, along with brief descriptions of the advances in knowledge they have provided. While clinical hyperpolarized [1-^{13}C]pyruvate MRI has many conceivable roles for improved management of patients, the current complexity of the imaging method, requirement of initial facility setup, and high running costs have limited translation of this technique into more widespread clinical use. Improving the technology to simplify translation, such as by streamlining delivery of tracer to the patient, is an area of active research that can help facilitate future multicenter trials and potentially routine clinical applications. This in turn could improve the feasibility of mass production of equipment and tracer similar to ^{18}F FDG and lead to reductions in the prices of study initiation and maintenance.

With hyperpolarized [1-^{13}C]pyruvate MRI, the detection of an early response to cancer treatment could be integrated into the patient management pathway, allowing targeted therapies and combinational treatments to be rapidly tailored for each patient as part of a personalized medical approach. Hyperpolarized [1-^{13}C]pyruvate MRI may also be used for the noninvasive evaluation of tumor grade or aggressiveness in selected patients where biopsy is challenging or to target biopsies to areas of high lactate to derive more accurate results (47).

Other promising applications of hyperpolarized ^{13}C MRI with potential for more immediate use involve combination with complementary imaging modalities such as ^{18}F-FDG PET (48) or emerging techniques such as deuterium metabolic imaging, where glucose is labeled with the ^{2}H isotope of hydrogen, thereby providing a more complete picture of cellular metabolism than each of these individual techniques alone (49,50).
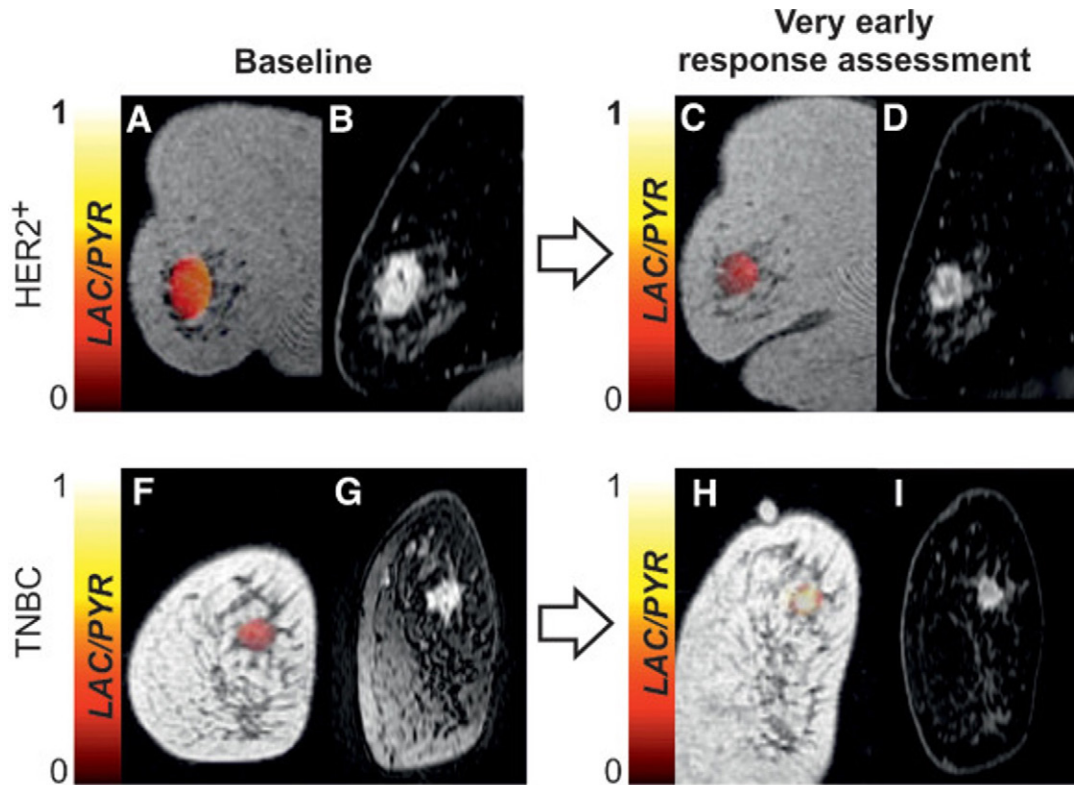
Figure 6: Two patients with human epidermal growth factor receptor 2–positive (HER2+) breast cancer (top row) and triple-negative breast cancer (TNBC) (bottom row). **(A, F)** Hyperpolarized carbon 13 MRI lactate:pyruvate (LAC/PYR) maps for both patients superimposed on hydrogen 1 MR images. **(B, G)** Diffusion images at baseline. Early follow-up **(C, H)** hyperpolarized and **(D, I)** diffusion images. Differences between baseline and follow-up images were significant for tumor volume and diffusivity. (Reprinted, under a CC BY 4.0 license, from reference 30.)

The standardized uptake value of ^{18}F FDG is higher in tumors because of an increase in metabolic activity, glucose transporter expression, and activity of the enzyme hexokinase which phosphorylates and traps the tracer intracellularly. Standardized uptake value is already used in clinical practice for treatment response monitoring as well as for the detection of new cancer and recurrence (51,52). ^{18}F-FDG PET and hyperpolarized [1-^{13}C] pyruvate MRI depict tissue metabolism in complementary ways and are sensitive to different steps in the metabolism of glucose, allowing these modalities to investigate different enzymes and transporters (3).

Where available, hybrid PET/MRI scanners can be used with ^{18}F-FDG and hyperpolarized [1-^{13}C]pyruvate MRI to further improve the metabolic phenotyping of tissue. ^{18}F-FDG PET images can be more accurately coregistered to hyperpolarized [1-^{13}C]pyruvate MRI with PET/MRI scanners than with PET/CT. Simultaneous ^{18}F-FDG PET and hyperpolarized [1-^{13}C]pyruvate MRI has already been performed in a canine cancer model which showed that hyperpolarized [1-^{13}C]pyruvate MRI was more specific for the Warburg effect, while ^{18}F-FDG PET could not differentiate between increased glucose uptake and the processes of oxidative phosphorylation and glycolysis (53).

Validation of the measurements of pyruvate and its metabolites in tissue using hyperpolarized [1-^{13}C]pyruvate MRI is challenging due to the large number of biologic covariates and the difficulty of rapidly halting chemical reactions in biologic systems to facilitate ex vivo quantification. To date, only few studies have provided tissue validation for the imaging measurements (16,20,54). Larger biologic and technical validation studies are required to understand the changes that drive signal generation in hyperpolarized ^{13}C MRI and to further evaluate the repeatability and reproducibility of the results, for which there have already been a few promising reports in specific tumors such as prostate cancer (26).

Conclusion

Hyperpolarized [1-^{13}C]pyruvate MRI has been extensively studied preclinically and has been successfully implemented in human studies at multiple clinical sites and across several cancers. The biologic mechanisms underlying the changes in imaging are tumor-specific and have been shown to include expression of the pyruvate transporter and the enzyme converting it into lactate as well as the endogenous tissue concentration of lactate. Early human research suggests that clinical hyperpolarized [1-^{13}C]pyruvate MRI may have the potential to fulfill the promise of preclinical results. In the human studies performed thus far, the technique has produced findings that have demonstrated an ability to stratify tumors based on their metabolic phenotype, more accurately detect multifocal disease, assist in tumor grading, and detect early response to therapy.

Hyperpolarized [1-^{13}C]pyruvate MRI remains a developing

Table 1: Selected Clinical Hyperpolarized Carbon 13 Pyruvate Studies in Oncology and Key Findings

Study	Tumor Studied	Focus of Study and/or Key Findings
Vaziri et al 2022 (55)	Glioblastoma	Demonstrated postprocessing denoising methods to improve SNR
Chen et al 2022 (56)	Prostate cancer	Proof-of-concept guide for fusion imaging in transrectal biopsies
Sushentsev et al 2022 (16)	Prostate cancer	HP [1-^{13}C] MRI had higher sensitivity at detecting intermediate grade prostate cancer than proton MRI
Zaccagna et al 2022 (20)	Glioblastoma	Tumor lactate heterogeneity demonstrated Tumor bicarbonate lower than surrounding brain
Ursprung et al 2022 (31)	Renal cell carcinoma	Differentiation of tumor by aggressiveness Expression of MCT-1 may be related to survival
Woitek et al 2021 (30)	Breast cancer	Detection of response to neoadjuvant chemotherapy
Autry et al 2020 (57)	Pediatric CNS cancers	Safety of imaging of pediatric population with CNS cancer
Woitek et al 2020 (41)	Breast cancer	Breast cancer response detected after one cycle of neoadjuvant chemotherapy
Autry et al 2020 (58)	Glioma	Rate constants elevated following bevacizumab treatment Progressive disease demonstrated elevated k_{PL}
Gallagher et al 2020 (18)	Breast cancer	Breast cancer demonstrated metabolic heterogeneity Lactate correlated with MCT-1 and hypoxia
Chen et al 2019 (59)	Prostate cancer metastases	Detected metabolism in metastases and changes following treatment
Tran et al 2019 (17)	Renal cell carcinoma	Assessment of metabolism and cancer heterogeneity
Gordon et al 2019 (8)	Prostate cancer and brain cancer	EPI acquisition provided whole-organ coverage while retaining high SNR and resolution
Larson et al 2018 (60)	Prostate cancer	Inputless k_{PL} fitting method for quantification of metabolism of HP [1-^{13}C]pyruvate demonstrated
Chen et al 2018 (61)	Prostate cancer	Feasibility of characterization of metabolism in animals and patients demonstrated
Park et al 2018 (62)	Brain tumor	Demonstrated safety and feasibility when evaluating in vivo brain metabolism
Aggarwal et al 2017 (63)	Prostate cancer	Illustrated potential as a biomarker of response
Nelson et al 2013 (10)	Prostate cancer	Confirmation of safety and demonstration of elevated [1-^{13}C]lactate and [1-^{13}C]pyruvate levels in cancer

Note.—^{13}C = carbon 13, CNS = central nervous system, EPI = echo-planar imaging, HP = hyperpolarized, k_{PL} = apparent exchange rate constant for lactate dehydrogenase, MCT-1 = monocarboxylate transporter 1, SNR = signal-to-noise ratio.

and improving technology. In the future, it may find use in clinical drug trials for monitoring responses to new treatments and in the identification of successful combinational regimens. The technique may also be improved by combination with ^{18}F-FDG PET and deuterium metabolic imaging to provide rich metabolic phenotypic information on tumors. Nevertheless, there remains a need for studies to undertake further biologic and technical validation as well as for larger multicenter trials to confirm results obtained from the proof-of-concept and small patient number studies that have been performed to date.

References

1. Ardenkjaer-Larsen JH, Fridlund B, Gram A, et al. Increase in signal-to-noise ratio of > 10,000 times in liquid-state NMR. Proc Natl Acad Sci USA 2003;100(18):10158–10163.
2. Couch MJ, Blasiak B, Tomanek B, et al. Hyperpolarized and inert gas MRI: the future. Mol Imaging Biol 2015;17(2):149–162.
3. Woitek R, Gallagher FA. The use of hyperpolarised ^{13}C-MRI in clinical body imaging to probe cancer metabolism. Br J Cancer 2021;124(7):1187–1198.
4. Wang ZJ, Ohliger MA, Larson PEZ, et al. Hyperpolarized 13C MRI: state of the art and future directions. Radiology 2019;291(2):273–284.
5. Chung BT, Chen HY, Gordon J, et al. First hyperpolarized [2-^{13}C]pyruvate MR studies of human brain metabolism. J Magn Reson 2019;309:106617.
6. Stewart NJ, Nakano H, Sugai S, et al. Hyperpolarized ^{13}C Magnetic Resonance Imaging of Fumarate Metabolism by Parahydrogen-induced Polarization: A Proof-of-Concept in vivo Study. ChemPhysChem 2021;22(10):915–923.
7. Qin H, Tang S, Riselli AM, et al. Clinical translation of hyperpolarized ^{13}C pyruvate and urea MRI for simultaneous metabolic and perfusion imaging. Magn Reson Med 2022;87(1):138–149.
8. Gordon JW, Chen HY, Autry A, et al. Translation of Carbon-13 EPI for hyperpolarized MR molecular imaging of prostate and brain cancer patients. Magn Reson Med 2019;81(4):2702–2709.
9. Wiesinger F, Weidl E, Menzel MI, et al. IDEAL spiral CSI for dynamic metabolic MR imaging of hyperpolarized [1-13C]pyruvate. Magn Reson Med 2012;68(1):8–16.
10. Nelson SJ, Kurhanewicz J, Vigneron DB, et al. Metabolic imaging of patients with prostate cancer using hyperpolarized [1-(1)(3)C]pyruvate. Sci Transl Med 2013;5:198ra108.

Table 2: Selected Preclinical Hyperpolarized Carbon 13 Pyruvate Studies in Oncology and Key Findings

Study	Tumor Studied	Model	Focus of Study and/or Key Findings
Lai et al 2021 (64)	Squamous cell carcinoma	Cell	Glycolytic alterations occur in response to irradiation
Park et al 2021 (65)	Glioma	Rodent	Distinct metabolic profiles for enhancing and nonenhancing gliomas
Choi et al 2021 (66)	Breast metastases to brain	Cell	Metformin therapy may affect k_{PL} in adjuvant treatment
Rao et al 2021 (67)	Pancreatic cancer, breast cancer	Cell	Injections of pyruvate may inhibit LDH activity
Kawai et al 2021 (68)	Glioblastoma	Cell	Increase in lactate:pyruvate ratio after irradiation
Macdonald et al 2021 (69)	Breast cancer	Cell	Potential for $AUC_{L/P}$ as biomarker of glycolytic metabolism
Perkons et al 2021 (70)	Hepatocellular carcinoma	Rat	Quantification of intratumoral metabolism is repeatable and reflective of intracellular processes
Park et al 2021 (71)	Glioma, metastases, and radiation necrosis	Mouse	Differentiation between radiation necrosis and brain tumors demonstrated
Fala et al 2021 (72)	Lymphoma	Mouse	Exchange between pyruvate and lactate correlates more with pyruvate delivery and less with endogenous lactate
Martinho et al 2020 (73)	Pancreatic cancer	Mouse	Higher lactate:pyruvate ratio in tumor Concern over distinguishing tumors from pancreatitis
van Heijster et al 2020 (74)	Prostate cancer	Mouse and cell	Metabolism in cell models differs from that in other tumor models such as mouse
Perkons et al 2020 (75)	Hepatocellular carcinoma	Rat	Quantification of intratumoral LDH pharmacodynamics and therapeutic efficacy prediction
Qin et al 2020 (76)	Prostate cancer	Mouse	HP ^{13}C-MRI findings can help monitor radiation-induced physiologic changes
Müller et al 2020 (77)	Breast cancer	Rat	Multiecho balanced SSFP improves resolution when compared with spectroscopy and FID
Lee et al 2020 (78)	Breast cancer	Rat	Lactate-to-pyruvate ratio correlates positively with [1-^{13}C]lactate measured from tissue extracts and negatively with tumor wet weight
Nivajärvi et al 2020 (79)	Glioma	Rat	Metabolic information gives a more comprehensive picture of gene therapy response
Acciardo et al 2020 (80)	Melanoma	Mouse	*BRAF* inhibition induced an increase in pyruvate-to-lactate ratio and in vivo conversion is influenced by tumor microenvironment
Mignion et al 2020 (81)	Head and neck SCC	Mouse	HP 13C-pyruvate is a potential marker for response to cetuximab
Michel et al 2019 (82)	Glioma	Mouse	Pyruvate metabolism can monitor treatment response
Feuerecker et al 2019 (83)	Bladder carcinoma	Cell	Lactate:pyruvate ratio detected early treatment response
Bachawal et al 2019 (84)	Prostate cancer	Canine	Simultaneous ^{13}C/PET/mpMRI and fusion-guided biopsy is feasible in a canine model
Radoul et al 2019 (85)	Glioblastoma	Mouse	Decrease in lactate production could serve as a biomarker of response to histone deacetylase inhibitors
Hundshammer et al 2018 (86)	Breast cancer	Rat	Variations in cell density affect PET and ^{13}C-MRI similarly Metabolic data may reflect both biochemistry and cellularity
Park et al 2019 (87)	Glioblastoma	Rat	HP ^{13}C MRI may be used to assess blood volume
Autry et al 2018 (88)	Pediatric DIPG	Rat	HP ^{13}C MRI may monitor biochemical processes in diffuse intrinsic pontine glioma
Lee et al 2019 (89)	Prostate cancer	Mouse	HP ^{13}C MRI in optimizing focal high-intensity focused ultrasound deserves further testing
Hansen et al 2018 (90)	Multiple canine cancers	Canine	Lactate and fluorine 18 FDG uptake can be related and depends on cancer type
Scroggins et al 2018 (91)	Prostate cancer	Mouse	HP [1-^{13}C]-pyruvate MRI findings help predict efficacy of targeting of the Warburg effect
Serrao et al 2018 (92)	Lymphoma	Mouse	Exchange between pyruvate and lactate can provide an estimate of the true isotope flux

(Table 2 continues)

Table 2 (continued): Selected Preclinical Hyperpolarized Carbon 13 Pyruvate Studies in Oncology and Key Findings

Study	Tumor Studied	Model	Focus of Study and/or Key Findings
Ravoori et al 2017 (48)	Ovarian cancer	Mouse	HP ^{13}C-pyruvate MRI may serve as an early indicator of response to tyrosine kinase inhibitors
Neveu et al 2016 (93)	Breast cancer and cervical cancer	Mouse	Discordance found in metabolic cancer cell bioenergetics between in vitro and in vivo setups
Chaumeil et al 2016 (94)	Glioma	Mouse	Metabolic imaging profile of mutant IDH1 gliomas could be used to detect the presence of the IDH1 mutation
Serrao et al 2016 (95)	Lymphoma	Mouse	The fasted state may be preferable for the measurement of ^{13}C label exchange
Düwel et al 2016 (96)	Hepatocellular carcinoma	Rat	Qualitative perfusion information can be extracted from fumarate and pyruvate imaging alone
Rajeshkumar et al 2015 (97)	Pancreatic cancer	Mouse	p53 status in pancreatic cancer can be a biomarker to predict sensitivity to LDH-A inhibition
Swisher et al 2014 (98)	Prostate cancer and liver cancer	Mouse and cell	Measurement of T1 values provides information about the environment of metabolites and can improve assessment of kinetics
Park et al 2013 (99)	Glioma	Rat	Demonstration of the feasibility of quantitatively detecting ^{13}C-bicarbonate in tumor-bearing rat brain
Park et al 2010 (100)	Brain tumors	Rat	Assessment of prognosis and monitoring response to therapy in brain tumors
Witney et al 2009 (101)	Lymphoma	Mouse	Comparison of HP [1-^{13}C]pyruvate MRI and fluorine 18 FDG PET/CT for measuring response to treatment
Day et al 2007 (40)	Lymphoma	Mouse	Early reduction in lactate labeling after treatment, explained by loss of NAD and decreases in tumor lactate and LDH

Note.—$AUC_{L/P}$ = area under the receiver operating characteristic curve ratio for lactate and pyruvate, ^{13}C = carbon 13, DIPG = diffuse intrinsic pontine glioma, FDG = fluorodeoxyglucose, FID = free induction decay, HP = hyperpolarized, IDH1 = isocitrate dehydrogenase 1, k_{PL} = apparent exchange rate constant for lactate dehydrogenase, LDH-A = lactate dehydrogenase A, mpMRI = multiparametric MRI, NAD = nicotinamide adenine dinucleotide, SCC = squamous cell carcinoma, SSFP = steady-state free precession.

11. Daniels CJ, McLean MA, Schulte RF, et al. A comparison of quantitative methods for clinical imaging with hyperpolarized (13)C-pyruvate. NMR Biomed 2016;29(4):387–399.
12. Schroeder MA, Cochlin LE, Heather LC, Clarke K, Radda GK, Tyler DJ. In vivo assessment of pyruvate dehydrogenase flux in the heart using hyperpolarized carbon-13 magnetic resonance. Proc Natl Acad Sci USA 2008;105(33):12051–12056.
13. Warburg O. On the origin of cancer cells. Science 1956;123(3191):309–314.
14. Gatenby RA, Gillies RJ. Why do cancers have high aerobic glycolysis? Nat Rev Cancer 2004;4(11):891–899.
15. Miloushev VZ, Granlund KL, Boltyanskiy R, et al. Metabolic imaging of the human brain with hyperpolarized 13C pyruvate demonstrates 13C lactate production in brain tumor patients. Cancer Res 2018;78(14):3755–3760.
16. Sushentsev N, McLean MA, Warren JB, et al. Hyperpolarised 13C-MRI identifies the emergence of a glycolytic cell population within intermediate-risk human prostate cancer. Nat Commun 2022;13(1):466. [Published correction appears in Nat Commun 2022;13(1):1274.]
17. Tran M, Latifoltojar A, Neves AY, et al. First-in-human in vivo non-invasive assessment of intra-tumoral metabolic heterogeneity in renal cell carcinoma. BJR Case Rep 2019;5(3):20190003.
18. Gallagher FA, Woitek R, McLean MA, et al. Imaging breast cancer using hyperpolarized carbon-13 MRI. Proc Natl Acad Sci USA 2020;117(4):2092–2098.
19. Stødkilde-Jørgensen H, Laustsen C, Hansen ESS, et al. Pilot Study Experiences With Hyperpolarized [1-13 C]pyruvate MRI in Pancreatic Cancer Patients. J Magn Reson Imaging 2020;51(3):961–963.
20. Zaccagna F, McLean MA, Grist JT, et al. Imaging Glioblastoma Metabolism by Using Hyperpolarized [1-^{13}C]Pyruvate Demonstrates Heterogeneity in Lactate Labeling: A Proof of Principle Study. Radiol Imaging Cancer 2022;4(4):e210076.
21. Walenta S, Mueller-Klieser WF. Lactate: mirror and motor of tumor malignancy. Semin Radiat Oncol 2004;14(3):267–274.
22. Walenta S, Wetterling M, Lehrke M, et al. High lactate levels predict likelihood of metastases, tumor recurrence, and restricted patient survival in human cervical cancers. Cancer Res 2000;60(4):916–921.
23. Dimopoulos MA, Barlogie B, Smith TL, Alexanian R. High serum lactate dehydrogenase level as a marker for drug resistance and short survival in multiple myeloma. Ann Intern Med 1991;115(12):931–935.
24. Keshari KR, Sriram R, Van Criekinge M, et al. Validation of Hyperpolarized 13C Lactate as a Prostate Cancer Biomarker Using a Human Prostate Tissue Slice Culture Bioreactor. International Society for Magnetic Resonance in Medicine. https://archive.ismrm.org/2013/3429.html. Published 2013.
25. Albers MJ, Bok R, Chen AP, et al. Hyperpolarized 13C lactate, pyruvate, and alanine: noninvasive biomarkers for prostate cancer detection and grading. Cancer Res 2008;68(20):8607–8615.
26. Granlund KL, Tee SS, Vargas HA, et al. Hyperpolarized MRI of human prostate cancer reveals increased lactate with tumor grade driven by monocarboxylate transporter 1. Cell Metab 2020;31(1):105–114.e3.
27. Halestrap AP, Price NT. The proton-linked monocarboxylate transporter (MCT) family: structure, function and regulation. Biochem J 1999;343(Pt 2):281–299.
28. Morris ME, Felmlee MA. Overview of the proton-coupled MCT (SLC16A) family of transporters: characterization, function and role in the transport of the drug of abuse gamma-hydroxybutyric acid. AAPS J 2008;10(2):311–321.
29. Harris T, Eliyahu G, Frydman L, Degani H. Kinetics of hyperpolarized 13C1-pyruvate transport and metabolism in living human breast cancer cells. Proc Natl Acad Sci USA 2009;106(43):18131–18136.
30. Woitek R, McLean MA, Ursprung S, et al. Hyperpolarized carbon-13 MRI for early response assessment of neoadjuvant chemotherapy in breast cancer patients. Cancer Res 2021;81(23):6004–6017.
31. Ursprung S, Woitek R, McLean MA, et al. Hyperpolarized ^{13}C-Pyruvate Metabolism as a Surrogate for Tumor Grade and Poor Outcome in Renal Cell Carcinoma-A Proof of Principle Study. Cancers (Basel) 2022;14(2):335.
32. Koukourakis MI, Giatromanolaki A, Sivridis E, et al; Tumour and Angiogenesis Research Group. Lactate dehydrogenase-5 (LDH-5) overexpression in non-small-cell lung cancer tissues is linked to tumour hypoxia, angiogenic factor production and poor prognosis. Br J Cancer 2003;89(5):877–885.
33. Koukourakis MI, Giatromanolaki A, Simopoulos C, Polychronidis A, Sivridis E. Lactate dehydrogenase 5 (LDH5) relates to up-regulated hypoxia induc-

ible factor pathway and metastasis in colorectal cancer. Clin Exp Metastasis 2005;22(1):25–30.

34. Kolev Y, Uetake H, Takagi Y, Sugihara K. Lactate dehydrogenase-5 (LDH-5) expression in human gastric cancer: association with hypoxia-inducible factor (HIF-1α) pathway, angiogenic factors production and poor prognosis. Ann Surg Oncol 2008;15(8):2336–2344.

35. Le A, Cooper CR, Gouw AM, et al. Inhibition of lactate dehydrogenase A induces oxidative stress and inhibits tumor progression. Proc Natl Acad Sci USA 2010;107(5):2037–2042.

36. Masoud GN, Li W. HIF-1α pathway: role, regulation and intervention for cancer therapy. Acta Pharm Sin B 2015;5(5):378–389.

37. Chen B, Zhang M, Xing D, Feng Y. Atorvastatin enhances radiosensitivity in hypoxia-induced prostate cancer cells related with HIF-1α inhibition. Biosci Rep 2017;37(4):BSR20170340.

38. Gurrapu S, Jonnalagadda SK, Alam MA, et al. Monocarboxylate transporter 1 inhibitors as potential anticancer agents. ACS Med Chem Lett 2015;6(5):558–561.

39. Kim EY, Chung TW, Han CW, et al. A novel lactate dehydrogenase inhibitor, 1-(phenylseleno)-4-(trifluoromethyl) benzene, suppresses tumor growth through apoptotic cell death. Sci Rep 2019;9(1):3969.

40. Day SE, Kettunen MI, Gallagher FA. Detecting tumor response to treatment using hyperpolarized 13C magnetic resonance imaging and spectroscopy. Nat Med 2007;13(11):1382–1387. [Published correction appears in Nat Med 2007;13(12):1521.]

41. Woitek R, McLean MA, Gill AB, et al. Hyperpolarized 13C MRI of tumor metabolism demonstrates early metabolic response to neoadjuvant chemotherapy in breast cancer. Radiol Imaging Cancer 2020;2(4):e200017.

42. Alano CC, Garnier P, Ying W, Higashi Y, Kauppinen TM, Swanson RA. NAD+ depletion is necessary and sufficient for poly(ADP-ribose) polymerase-1-mediated neuronal death. J Neurosci 2010;30(8):2967–2978.

43. Ma Y, Chen H, Xia W, Ying W. Oxidative stress and PARP activation mediate the NADH-induced decrease in glioma cell survival. Int J Physiol Pathophysiol Pharmacol 2011;3(1):21–28.

44. Wang ZH, Peng WB, Zhang P, Yang XP, Zhou Q. Lactate in the tumour microenvironment: From immune modulation to therapy. EBioMedicine 2021;73:103627.

45. Chang C-H, Pearce EL. Emerging concepts of T cell metabolism as a target of immunotherapy. Nat Immunol 2016;17(4):364–368.

46. Kouidhi S, Ben Ayed F, Benammar Elgaaied A. Targeting tumor metabolism: a new challenge to improve immunotherapy. Front Immunol 2018;9:353.

47. Sushentsev N, McLean MA, Warren AY, et al. The potential of hyperpolarised 13C-MRI to target glycolytic tumour core in prostate cancer. Eur Radiol 2022;32(10):7155–7162.

48. Ravoori MK, Singh SP, Lee J, Bankson JA, Kundra V. In vivo assessment of ovarian tumor response to tyrosine kinase inhibitor pazopanib by using hyperpolarized 13C-pyruvate MR spectroscopy and 18F-FDG PET/CT imaging in a mouse model. Radiology 2017;285(3):830–838.

49. De Feyter HM, Behar KL, Corbin ZA, et al. Deuterium metabolic imaging (DMI) for MRI-based 3D mapping of metabolism in vivo. Sci Adv 2018;4(8):eaat7314.

50. Kaggie JD, Khan AS, Matys T, et al. Deuterium metabolic imaging and hyperpolarized 13C-MRI of the normal human brain at clinical field strength reveals differential cerebral metabolism. Neuroimage 2022;257:119284.

51. Avril N, Sassen S, Schmalfeldt B, et al. Prediction of response to neoadjuvant chemotherapy by sequential F-18-fluorodeoxyglucose positron emission tomography in patients with advanced-stage ovarian cancer. J Clin Oncol 2005;23(30):7445–7453.

52. Thrall MM, DeLoia JA, Gallion H, Avril N. Clinical use of combined positron emission tomography and computed tomography (FDG-PET/CT) in recurrent ovarian cancer. Gynecol Oncol 2007;105(1):17–22.

53. Gutte H, Hansen AE, Henriksen ST, et al. Simultaneous hyperpolarized (13) C-pyruvate MRI and (18)F-FDG-PET in cancer (hyperPET): feasibility of a new imaging concept using a clinical PET/MRI scanner. Am J Nucl Med Mol Imaging 2014;5(1):38–45.

54. Keshari KR, Sriram R, Van Criekinge M, et al. Metabolic reprogramming and validation of hyperpolarized 13C lactate as a prostate cancer biomarker using a human prostate tissue slice culture bioreactor. Prostate 2013;73(11):1171–1181.

55. Vaziri S, Autry AW, Lafontaine M, et al. Assessment of higher-order singular value decomposition denoising methods on dynamic hyperpolarized [1-13C]pyruvate MRI data from patients with glioma. Neuroimage Clin 2022;36:103155.

56. Chen HY, Bok RA, Cooperberg MR, et al. Improving multiparametric MR-transrectal ultrasound guided fusion prostate biopsies with hyperpolarized 13C pyruvate metabolic imaging: A technical development study. Magn Reson Med 2022;88(6):2609–2620.

57. Autry AW, Park I, Kline C, et al. Pilot study of hyperpolarized 13C metabolic imaging in pediatric patients with diffuse intrinsic pontine glioma and other CNS cancers. AJNR Am J Neuroradiol 2021;42(1):178–184.

58. Autry AW, Gordon JW, Chen HY, et al. Characterization of serial hyperpolarized 13C metabolic imaging in patients with glioma. Neuroimage Clin 2020;27:102323.

59. Chen HY, Aggarwal R, Bok RA, et al. Hyperpolarized 13C-pyruvate MRI detects real-time metabolic flux in prostate cancer metastases to bone and liver: a clinical feasibility study. Prostate Cancer Prostatic Dis 2020;23(2):269–276.

60. Larson PEZ, Chen HY, Gordon JW, et al. Investigation of analysis methods for hyperpolarized 13C-pyruvate metabolic MRI in prostate cancer patients. NMR Biomed 2018;31(11):e3997.

61. Chen HY, Larson PEZ, Gordon JW, et al. Technique development of 3D dynamic CS-EPSI for hyperpolarized 13C pyruvate MR molecular imaging of human prostate cancer. Magn Reson Med 2018;80(5):2062–2072.

62. Park I, Larson PEZ, Gordon JW, et al. Development of methods and feasibility of using hyperpolarized carbon-13 imaging data for evaluating brain metabolism in patient studies. Magn Reson Med 2018;80(3):864–873.

63. Aggarwal R, Vigneron DB, Kurhanewicz J. Hyperpolarized 1-[13C]-pyruvate magnetic resonance imaging detects an early metabolic response to androgen ablation therapy in prostate cancer. Eur Urol 2017;72(6):1028–1029.

64. Lai YC, Hsieh CY, Lu KY, et al. Monitoring Early Glycolytic Flux Alterations Following Radiotherapy in Cancer and Immune Cells: Hyperpolarized Carbon-13 Magnetic Resonance Imaging Study. Metabolites 2021;11(8):518.

65. Park S, Rintaro H, Kim SK, Park I. Characterization of distinctive in vivo metabolism between enhancing and non-enhancing gliomas using hyperpolarized carbon-13 MRI. Metabolites 2021;11(8):504.

66. Choi YS, Lee J, Lee HS, Song JE, Kim DH, Song HT. Offset of apparent hyperpolarized 13C lactate flux by the use of adjuvant metformin in ionizing radiation therapy in vivo. NMR Biomed 2021;34(8):e4561.

67. Rao Y, Gammon ST, Sutton MN, Zacharias NM, Bhattacharya P, Piwnica-Worms D. Excess exogenous pyruvate inhibits lactate dehydrogenase activity in live cells in an MCT1-dependent manner. J Biol Chem 2021;297(1):100775.

68. Kawai T, Brender JR, Lee JA, et al. Detection of metabolic change in glioblastoma cells after radiotherapy using hyperpolarized 13C-MRI. NMR Biomed 2021;34(7):e4514.

69. Macdonald EB, Begovatz P, Barton GP, et al. Hyperpolarized 13C Magnetic Resonance Spectroscopic Imaging of Pyruvate Metabolism in Murine Breast Cancer Models of Different Metastatic Potential. Metabolites 2021;11(5):274.

70. Perkons NR, Johnson O, Pilla G, Gade TPF. Pharmacodynamics and pharmacokinetics of hyperpolarized [1-13C]-pyruvate in a translational oncologic model. NMR Biomed 2021;34(6):e4502.

71. Park I, Kim S, Pucciarelli D, et al. Differentiating radiation necrosis from brain tumor using hyperpolarized carbon-13 MR metabolic imaging. Mol Imaging Biol 2021;23(3):417–426.

72. Fala M, Somai V, Dannhorn A, et al. Comparison of 13C MRI of hyperpolarized [1-13C]pyruvate and lactate with the corresponding mass spectrometry images in a murine lymphoma model. Magn Reson Med 2021;85(6):3027–3035.

73. Martinho RP, Bao Q, Markovic S, et al. Identification of variable stages in murine pancreatic tumors by a multiparametric approach employing hyperpolarized 13C MRSI, 1H diffusivity and 1H T1 MRI. NMR Biomed 2021;34(2):e4446.

74. van Heijster FHA, Heskamp S, Breukels V, et al. Pyruvate-lactate exchange and glucose uptake in human prostate cancer cell models. A study in xenografts and suspensions by hyperpolarized [1-13C]pyruvate MRS and [18F] FDG-PET. NMR Biomed 2020;33(10):e4362.

75. Perkons NR, Johnson O, Pilla G, et al. Functional Genetic Screening Enables Theranostic Molecular Imaging in Cancer. Clin Cancer Res 2020;26(17):4581–4589.

76. Qin, H, Zhang V, Bok RA, et al. Simultaneous Metabolic and Perfusion Imaging Using Hyperpolarized 13C MRI Can Evaluate Early and Dose-Dependent Response to Radiation Therapy in a Prostate Cancer Mouse Model. Int J Radiat Oncol Biol Phys 2020;107(5):887–896.

77. Müller CA, Hundshammer C, Braeuer M, et al. Dynamic 2D and 3D mapping of hyperpolarized pyruvate to lactate conversion in vivo with efficient multi-echo balanced steady-state free precession at 3 T. NMR Biomed 2020;33(6):e4291.

78. Lee CY, Lau JYC, Geraghty BJ, Chen AP, Gu YP, Cunningham CH. Correlation of hyperpolarized 13C-MRI data with tissue extract measurements. NMR Biomed 2020;33(5):e4269.

79. Nivajärvi R, Olsson V, Hyppönen V, et al. Detection of lentiviral suicide gene therapy in C6 rat glioma using hyperpolarised [1-13C]pyruvate. NMR Biomed 2020;33(4):e4250.

80. Acciardo S, Mignion L, Lacomblez E, et al. Metabolic imaging using hyperpolarized 13C-pyruvate to assess sensitivity to the B-Raf inhibitor

vemurafenib in melanoma cells and xenografts. J Cell Mol Med 2020;24(2):1934–1944.

81. Mignion L, Acciardo S, Gourgue F, et al. Metabolic Imaging Using Hyperpolarized Pyruvate-Lactate Exchange Assesses Response or Resistance to the EGFR Inhibitor Cetuximab in Patient-Derived HNSCC Xenografts. Clin Cancer Res 2020;26(8):1932–1943.

82. Michel KA, Zieliński R, Walker CM, et al. Hyperpolarized pyruvate MR spectroscopy depicts glycolytic inhibition in a mouse model of glioma. Radiology 2019;293(1):168–173.

83. Feuerecker B, Michalik M, Hundshammer C, et al. Assessment of ^{213}Bi-anti-EGFR MAb treatment efficacy in malignant cancer cells with [1-^{13}C] pyruvate and [^{18}F]FDG. Sci Rep 2019;9(1):8294.

84. Bachawal SV, Park JM, Valluru KS, et al. Multimodality hyperpolarized C-13 MRS/PET/multiparametric MR imaging for detection and image-guided biopsy of prostate cancer: first experience in a canine prostate cancer model. Mol Imaging Biol 2019;21(5):861–870.

85. Radoul M, Najac C, Viswanath P, et al. HDAC inhibition in glioblastoma monitored by hyperpolarized ^{13}C MRSI. NMR Biomed 2019;32(2):e4044.

86. Hundshammer C, Braeuer M, Müller CA, et al. Simultaneous characterization of tumor cellularity and the Warburg effect with PET, MRI and hyperpolarized 13C-MRSI. Theranostics 2018;8(17):4765–4780.

87. Park I, Lupo JM, Nelson SJ. Correlation of tumor perfusion between carbon-13 imaging with hyperpolarized pyruvate and dynamic susceptibility contrast MRI in pre-clinical model of Glioblastoma. Mol Imaging Biol 2019;21(4):626–632.

88. Autry AW, Hashizume R, James CD, Larson PEZ, Vigneron DB, Park I. Measuring tumor metabolism in pediatric diffuse intrinsic pontine glioma using hyperpolarized carbon-13 MR metabolic imaging. Contrast Media Mol Imaging 2018;2018:3215658.

89. Lee JE, Diederich CJ, Bok R, et al. Assessing high-intensity focused ultrasound treatment of prostate cancer with hyperpolarized 13 C dual-agent imaging of metabolism and perfusion. NMR Biomed 2019;32(10):e3962.

90. Hansen AE, Gutte H, Holst P, et al. Combined hyperpolarized 13C-pyruvate MRS and 18F-FDG PET (hyperPET) estimates of glycolysis in canine cancer patients. Eur J Radiol 2018;103:6–12.

91. Scroggins BT, Matsuo M, White AO, et al. Hyperpolarized [1-13C]-pyruvate magnetic resonance spectroscopic imaging of prostate cancer in vivo predicts efficacy of targeting the Warburg effect. Clin Cancer Res 2018;24(13):3137–3148.

92. Serrao EM, Kettunen MI, Rodrigues TB, et al. Analysis of ^{13}C and ^{14}C labeling in pyruvate and lactate in tumor and blood of lymphoma-bearing mice injected with ^{13}C- and ^{14}C-labeled pyruvate. NMR Biomed 2018;31(5):e3901.

93. Neveu MA, De Preter G, Joudiou N, et al. Multi-modality imaging to assess metabolic response to dichloroacetate treatment in tumor models. Oncotarget 2016;7(49):81741–81749.

94. Chaumeil MM, Radoul M, Najac C, et al. Hyperpolarized (13)C MR imaging detects no lactate production in mutant IDH1 gliomas: Implications for diagnosis and response monitoring. Neuroimage Clin 2016;12:180–189.

95. Serrao EM, Rodrigues TB, Gallagher FA, et al. Effects of fasting on serial measurements of hyperpolarized [1-(13) C]pyruvate metabolism in tumors. NMR Biomed 2016;29(8):1048–1055.

96. Düwel S, Durst M, Gringeri CV, et al. Multiparametric human hepatocellular carcinoma characterization and therapy response evaluation by hyperpolarized (13) C MRSI. NMR Biomed 2016;29(7):952–960.

97. Rajeshkumar NV, Dutta P, Yabuuchi S, et al. Therapeutic Targeting of the Warburg Effect in Pancreatic Cancer Relies on an Absence of p53 Function. Cancer Res 2015;75(16):3355–3364.

98. Swisher CL, Larson PE, Kruttwig K, et al. Quantitative measurement of cancer metabolism using stimulated echo hyperpolarized carbon-13 MRS. Magn Reson Med 2014;71(1):1–11.

99. Park JM, Recht LD, Josan S, et al. Metabolic response of glioma to dichloroacetate measured in vivo by hyperpolarized (13)C magnetic resonance spectroscopic imaging. Neuro-oncol 2013;15(4):433–441.

100. Park I, Larson PE, Zierhut ML, et al. Hyperpolarized 13C magnetic resonance metabolic imaging: application to brain tumors. Neuro-oncol 2010;12(2):133–144.

101. Witney TH, Kettunen MI, Day SE, et al. A comparison between radiolabeled fluorodeoxyglucose uptake and hyperpolarized (13)C-labeled pyruvate utilization as methods for detecting tumor response to treatment. Neoplasia 2009;11(6):574–582.